



A novel collaborative study of abnormal roof water inrush in coal seam mining based on strata separation and wing crack initiation

Zaiyong Wang ^{a,b}, Qi Zhang ^{c,*}, Wenquan Zhang ^a

^a College of Energy and Mining Engineering, Shandong University of Science and Technology, Qingdao 266590, China

^b Key Laboratory of In-Situ Property-Improving Mining of Ministry of Education, Taiyuan University of Technology, Taiyuan 030024, China

^c Department of Civil and Environmental Engineering, The Hong Kong Polytechnic University, Hung Hom, Kowloon, Hong Kong, China



ARTICLE INFO

Keywords:

Roof water inrush
Bed separation space
Wing-crack initiation angle
Similar simulation experiment
T-stress

ABSTRACT

Separation water inrush poses a potential threat to safe mining on the working face, whose mechanism should be investigated in order to take better prevention and control measures. In this study, aiming at the problem of separation water inrush under hydrostatic pressure, the 21805 working face of the Yushujing coal mine was chosen as the research object to establish an in-house similar simulation experiment. The experiment could reveal the evolution law of bed separation space, the process of water accumulation in bed separation space, and the breaking characteristics of separation water inrush. Meanwhile, in order to theoretically interpret the evolution of water-conducting fractured zone (WCFZ), an analytical model for wing crack initiation from compression-shear fracture and tension-shear fracture that considers T-stress was derived. The analytical model comprehensively considers the effects of overlying strata load and aquifer water pressure, fracture geometry, and rock properties. The results show that the time of separation water inrush obtained by the similar simulation experiment is consistent with the field result, and the orientation of new cracks generated due to water injection also coincides with the analytical solution. In addition, it is found that the development of bed separation space is a long-term process, which can provide a theoretical basis for the prevention and control of separation water inrush.

1. Introduction

The mining of underground coal resources [6,18] leads to subsidence and even collapse of overlying strata. Due to the significant difference in bending strength of different rocks, transverse cracks would be formed between adjacent strata. With the further advancement of the working face, the un-synchronous bending deflections become more and more evident and finally lead to a separation layer [1,2], which is also known as the bed separation space [12,40]. Most of the bed separation space will disappear with the movement of surrounding rocks, while only the bed separation space above the water-conducting fractured zone (WCFZ) can be stably developed for a long time to form a larger bed separation space. During this process, the groundwater in the upper sandstone layer would gradually transport into the bed separation space through pores and fissures. As a result, a large amount of groundwater accumulates in the separation space from surrounding aquifers, causing hydrostatic pressure on the lower strata. With the increase of hydrostatic pressure and overlying strata load, mining-induced fractures would propagate and increase the range of WCFZ [3,22,31],

* Corresponding author.

E-mail address: q7zhang@polyu.edu.hk (Q. Zhang).

and when the water-conducting vertical fractures reach the bed separation space, abnormal water inrush could happen, seriously threatening the people and equipment on the working face [5,19,26,36,42,45].

Compared with other water disasters in coal mines, separation water inrush has the characteristics of no obvious surge sign and instantaneous flooding with a large volume of water, which make it difficult to prevent and control effectively. To ensure the safe production, a lot of research has been done on the identification methods and prevention measures of separation water inrush such as the grouting technology [19,50]. Gui et al. [8] studied the important factors affecting the formation of separation water from the perspective of geological conditions and mining conditions, and they proposed many prevention measures including interception, diversion, destruction of the buffer layer, grouting, and backfilling. On the basis of these techniques, the key stratum theory was used to identify the development location of the bed separation space. For engineering application, the geological conditions of the 1307 working face in Xinji No. 1 coal mine of Huainan (Anhui Province) were taken as an example, and the theoretical calculation results were consistent with the actual situation [7]. Li et al. [15] obtained the development location of the bed separation space in Hongliu coal mine by using field drilling and color television techniques. Groundwater accumulation at this location was detected by the whole-space transient electromagnetic method. Hu et al. [10] developed the trapezoidal platform model suitable for the breakage of the overlying strata. The evolution process and geometry shape of bed separation space were analyzed. In addition, the plate theory was used to reveal the relationship between the breakage of the overlying strata and separation water inrush. Wu et al. [35] developed the rock plate method to determine the development location and maximum height of the bed separation space. This method has been applied in Yuanzigou coal mine, and the result was consistent with the result from the field drilling video. Wang et al. [33] developed a new type of similar material from river sand, nanosized calcium carbonate, model gypsum, and aqueous paraffin wax emulsion. Different lithological strata were simulated according to different proportions of material components. The successful development of this material provides an opportunity to visualize the process of separation water inrush of Hongliu coal mine. In fact, the method of similar experiment has already been used in the mining engineering to measure the floor pore water pressure [43,46], stress and displacement of the overburden strata [32,38], and so on.

However, there are still few studies on the mechanical model of separation water inrush. In particular, the analytical model of separation water inrush caused by hydrostatic pressure, or caused by the combined action of hydrostatic pressure and overlying strata, is still not yet sophisticated. By using the beam theory, Qiao et al. [24] constructed the model of separation water inrush under hydrostatic pressure, and the corresponding maximum height of rock beam was also obtained. However, the mining-induced cracks were not considered in their model, which could make their results less conservative. Therefore, a theoretical model that quantitatively analyzes the impacts of new cracks induced by the overburden load and hydrostatic pressure on the evolution of WCFZ is deemed to be necessary, and it will also enrich the experimental results.

The paper is organized as follows. In Section 2, we briefly introduced the background information of the study site. Subsequently in Sections 3 and 4, laboratory similar simulation experiment and an analytical model of wing crack initiation (a prerequisite for separation water inrush) were described, respectively. In Section 5, comprehensive results were discussed in detail, which include the reliability of the analytical model comparing with the experimental observations, the evolution law of bed separation space, the

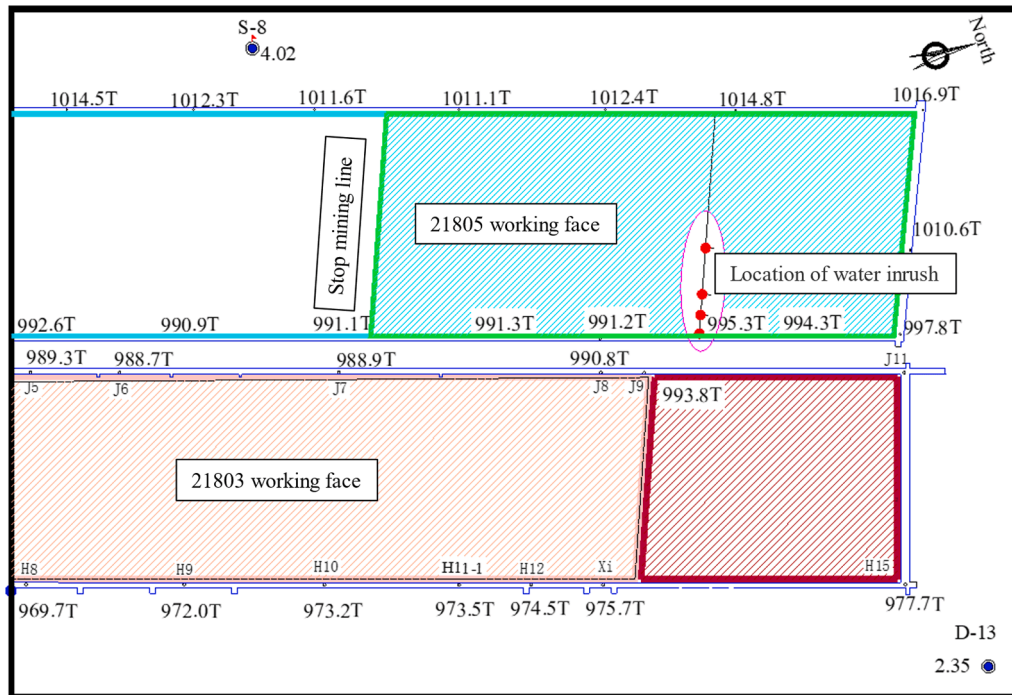


Fig. 1. Layout map of the 21805 working face. The number next to the borehole represents the thickness of the coal seam (m).

process of water accumulation in bed separation space, and the damage of separation water inrush. Important conclusions and comments were given in [Section 6](#). This study will be helpful for understanding the crack initiation mechanism and predicting the time of separation water inrush for other similar coal mines.

2. Engineering background of the study site

Yushujing coal mine is located at the border of Inner Mongolia Autonomous Region and Ningxia Hui Autonomous Region, belonging to the northwest part of Ordos Basin. The minefield is distributed in a banded shape with an area of 24.5561 km². The minefield is 7.4 km long (from north to south) and 2.9 ~ 4.1 km wide (from east to west). The elevation of the coal seam mining depth is from -1100 m to -560 m.

The 21805 working face is located at the north wing of the minefield, which belongs to the No. 8 coal seam of Jurassic Yan'an formation. The width of the working face is 160 m, the mining advancing length is 381 m, and the recoverable reserve is 210,000 tons. The detailed location information of the 21805 working face is given as follows: the 21803 working face is to the east of the 21805 working face with a 20 m coal pillar isolation distance, the protective coal pillar of S-8 hydrological borehole is to the south of this working face, the minefield boundary is to the west of this working face, and the north area is intact. The minimum distance from the open cut of the working face to the Zhiluo formation is about 30.4 m, and the minimum distance to the Cretaceous system is about 71.4 m. There is no fault near the working face, and the fault is also not found during the roadway excavation. The layout map of the 21805 working face is shown in [Fig. 1](#) and the overburden strata comprehensive borehole histogram is shown in [Fig. 2](#).

The trial production of the 21805 working face began on September 16th, 2019. On November 5th, 2019, when the working face was pushed to 88.7 m, the roof of the middle and lower supports was sprayed with water, and the flow rate suddenly increased to 130 m³/h. Since then, the water flow rate in the working face began to decay, and on November 15th, the flow rate decreased to 35 m³/h

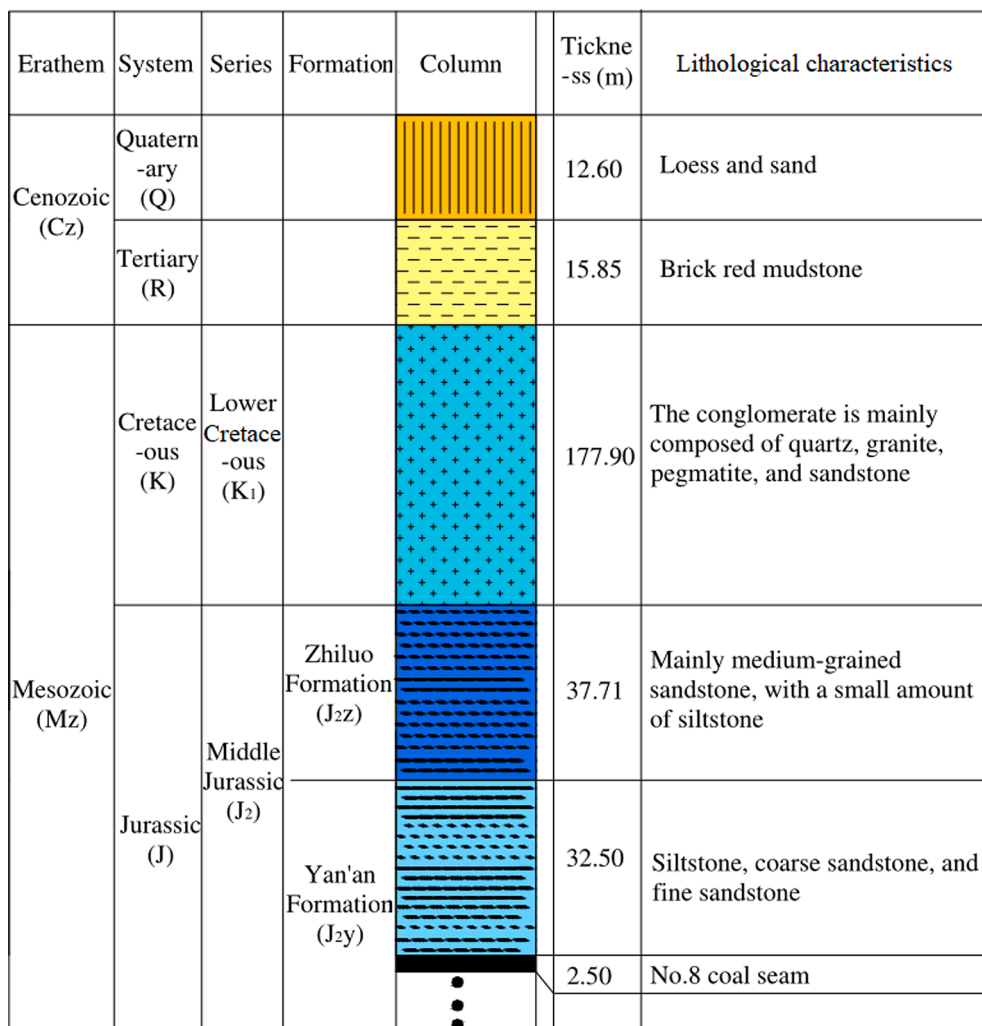


Fig. 2. Overburden strata comprehensive borehole histogram of the 21805 working face.

and the production was restored. On November 29th, there was almost no water production in the whole working face.

By means of hydro-chemical analysis, it was found that the water inrush occurred in the working face involved the sandstone water in Zhiluo formation. This was also confirmed by the observation data from the S-8 hydrological borehole in Zhiluo formation, the groundwater table was significantly decreased, as shown in Fig. 3. The time of rapid drop in the groundwater table was consistent with the time of water inrush at the working face. Therefore, the accident was identified as the separation water inrush accident, and the source of the separation water was the aquifer in Zhiluo formation.

We try to study this water inrush accident from theoretical and experimental perspectives. For the theoretical perspective, we explore the wing crack initiation criterions and try to find the reasonable crack initiation angle. However, the dynamic evolutions of bed separation space and WCFZ can only be analyzed and better understood by similar experiment. The consistency between the theoretical prediction and the experimental phenomenon should also be addressed. All of these details are given in the following sections.

3. Similar simulation experiment preparation

A two-dimensional similar simulation experiment in the laboratory could be a feasible approach to better understand the process of strata separation and separation water inrush [27,28,41]. By adopting the 21805 working face introduced in Section 2 as our research object (prototype), a physical model with a length of 250 cm, a thickness of 30 cm, and a height of 162.5 cm was established, and the geometric similarity ratio was 1/80. Note in the definition of similarity ratio, we always put the quantity of the similar model on the numerator, while we put the quantity of the prototype on the denominator. Besides the geometric similarity ratio, other relevant similarity ratios were also given here: similarity ratio of time was 1/9; similarity ratio of solid density was 1/1.5; similarity ratio of fluid density was 1/1; similarity ratio of strength (same for the elastic modulus) was 1/120; similarity ratio of Poisson's ratio was 1/1; similarity ratio of hydraulic conductivity was 1/9.

The model mainly consists of a multi-angle physical simulation test system, a groundwater seepage simulation system, and a separation water recovery system. The geometric size of the model frame was set to be 2.5 m × 0.3 m × 2.2 m, and the maximum model laying height reached 1.9 m. A top hydraulic jack was used for pressure loading of the geometric model. DH3815 and DH3818 strain testing machines produced by the Jiangsu Donghua Testing Instrument Co., Ltd. were used to monitor the stress changes at the established monitoring points. The Nanfang NTS-391R10 total station was selected to monitor the subsidence movement of the overlying strata. To simulate the groundwater seepage process in similar materials (rock strata and coal seam), it is necessary to provide an appropriate material equation/ratio considering the water-resistance effect. Fortunately, this part was completed in our previous work [33]. In addition, the water source of the model was provided through a small peristaltic pump DIPump550-B253 and an inlet pipe. The small peristaltic pump includes a digital display panel, stepper motor, forward and reverse switches, speed control knob, and pedal switch. The flow rate of the pump ranged from 5 mL/min to 670 mL/min. Two water collectors were arranged outside the model to collect water flowing out from the working face. An overview of the physical model is shown in Fig. 4.

In the paving process of the model, mica powder was spread to prevent rock strata from bonding, as shown in Fig. 5(a). The paving and proportioning of similar materials are provided in Table 1. The water inlet pipeline was deeply buried within the model, and the burial method entailed vertical arrangement. The distance between adjacent pipelines was 10 cm. The pipeline outlet was located in the 9th layer of coarse sandstone, and the pipeline inlet was located at the top of the model and was connected with a water-conducting

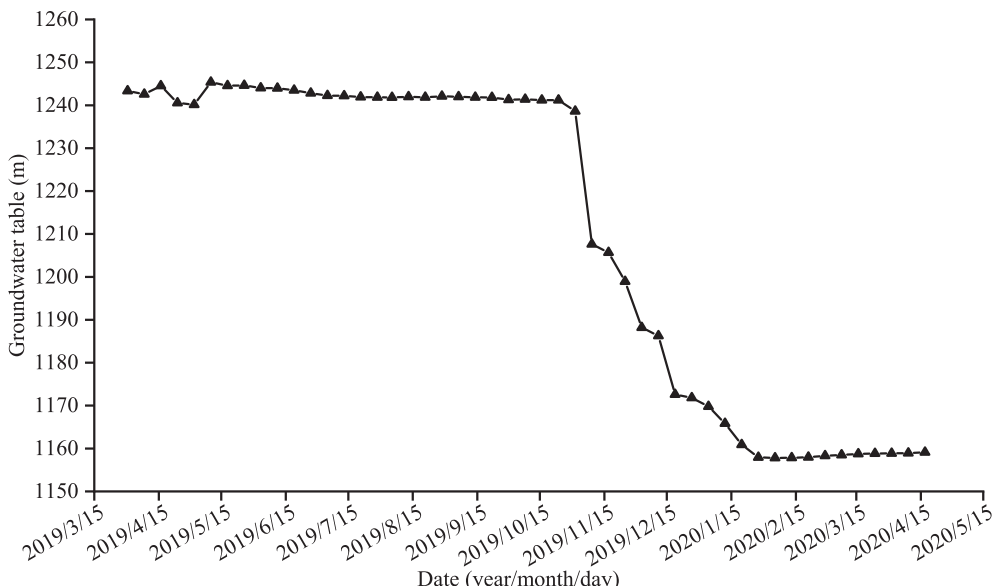


Fig. 3. Groundwater table variation during the observation time from S-8 hydrological borehole in Zhiluo formation.

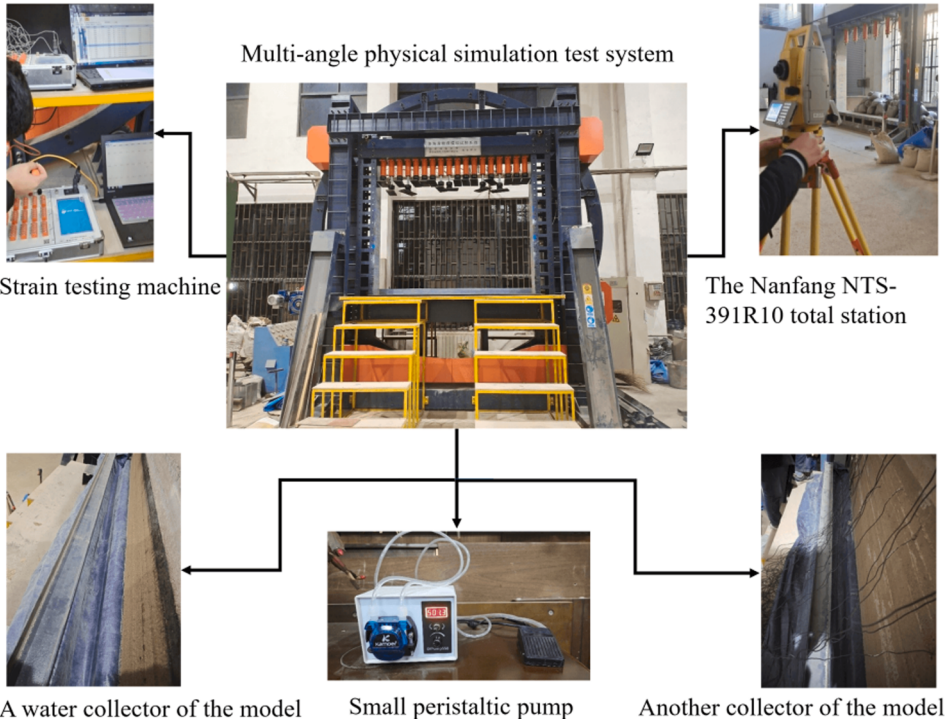


Fig. 4. An overview of the physical model.

hose, as shown in Fig. 5(c). To monitor the stress change in the overlying strata during the advancing process of the coal seam, 24 stress sensors were arranged in this experiment, which were located in the 4th fine sandstone layer, the 8th siltstone layer, and the 9th coarse sandstone layer.

After model drying, reflectors were installed on the surface of the model. The horizontal distance between two adjacent reflectors was 5 cm and the vertical distance was 10 cm. Strata were distinguished with different colors (from the 3rd layer to the 11th layer), in which black indicates coal seam, white indicates fine sandstone, red indicates coarse sandstone, and blue indicates siltstone. When a stable separation space formed in the overlying strata, water was injected into the model through the pipeline injection system. The water accumulation trend and seepage characteristics of the bed separation space under the influence of mining were observed. Water collectors were used to collect water discharged from the working face in the experiment. The total working face advancing length was 150 cm, starting from the right side of the model, and each advancing distance was 10 cm. According to the geometric similarity ratio, the corresponding actual advancing distance of the working face was 8 m. If the actual daily advancing speed in the coal mine reached approximately 5 m/d, according to the time similarity ratio, 10 cm of model advancement occurred every 4.3 h.

4. Analytical solution of wing crack initiation

Wing crack initiation and propagation is a critical factor during the process of separation water inrush. Therefore, besides the similar simulation experiment in laboratory, we want to derive some analytical results for the problem of wing crack initiation induced by the combined action of water pressure and overlying strata load. Latter these results can be used as references for the interpretation of the laboratory experimental results.

We take the element from the strata below the bed separation space with one inclined crack as our analysis object, as shown in Fig. 6. The far-field compressive stress σ_m , far-field normal stress σ_n , and far-field shear stress τ are given as [17]

$$\sigma_m = \sigma(\sin^2\alpha + \zeta\cos^2\alpha) \quad (1)$$

$$\sigma_n = \sigma(\cos^2\alpha + \zeta\sin^2\alpha) \quad (2)$$

$$\tau = \sigma(1 - \zeta)\sin\alpha\cos\alpha \quad (3)$$

where σ is the vertical stress, ζ is the lateral stress coefficient, and α is the inclination angle (with horizon). In this study, we assume the singular stress field at the fracture tip still belongs to the type of mixed I-II mode, and the asymptotic stress field in the vicinity of the crack tip can be generally expressed in the local $r\&\theta$ system (polar coordinate) as [20]

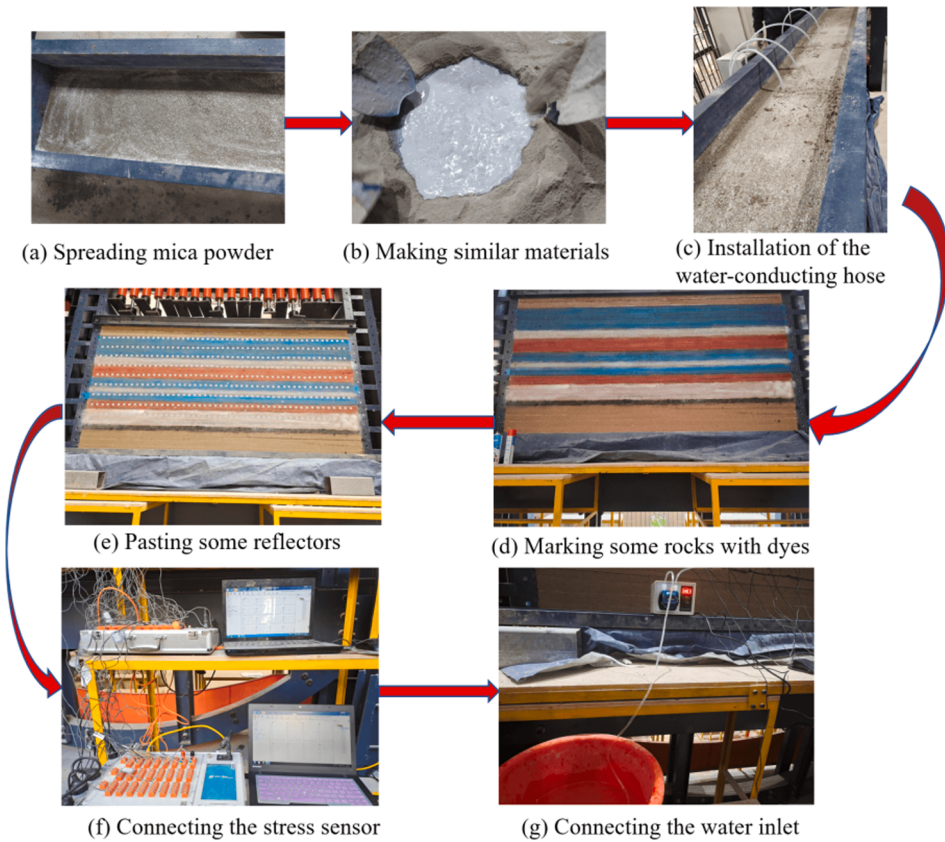


Fig. 5. The set-up process of the similar model and the test system.

Table 1

Proportions of all constituents in the similar experiment. Note that the No. 1 stratum represents the lowest stratum in the model.

Rock stratum number	Lithological characters	Actual thickness/m	Model thickness/cm	Solid mass /kg					Liquid mass /kg	
				River sand	Nanosized calcium carbonate	Model gypsum	Ca-bentonite	Total mass	Water	Aqueous paraffin wax emulsion
13	Siltstone	6	7.5	96.55	5.52	6.90	1.38	110.35	3.31	7.72
12	Fine sandstone	6	7.5	96.55	11.04	2.76	0	110.35	8.83	2.21
11	Siltstone	18	22.5	289.69	16.55	20.69	4.14	331.07	9.93	23.17
10	Fine sandstone	7	8.75	112.65	12.87	3.22	0	128.74	10.30	2.57
9	Coarse sandstone	10	12.5	153.26	9.20	21.45	0	183.91	16.55	1.84
8	Siltstone	8	10	128.74	7.36	9.20	1.84	147.14	4.41	10.30
7	Fine sandstone	4	5	64.37	7.36	1.84	0	73.57	5.89	1.47
6	Siltstone	6	7.5	96.55	5.52	6.90	1.38	110.35	3.31	7.72
5	Coarse sandstone	6	7.5	91.96	5.52	12.87	0	110.35	9.93	1.10
4	Fine sandstone	12	15	193.12	22.07	5.52	0	220.71	17.66	4.41
3	No. 8 coal seam	3	3.75	47.30	5.52	2.36	0	55.18	5.52	0
2	Siltstone	20	25	321.87	18.39	22.99	4.60	367.85	11.04	25.75
1	Fine sandstone	24	30	386.24	44.14	11.04	0	441.42	35.31	8.83

$$\sigma_r(r, \theta) = \frac{1}{2\sqrt{2\pi}r} \left[K_I(3 - \cos\theta)\cos\frac{\theta}{2} + K_H(3\cos\theta - 1)\sin\frac{\theta}{2} \right] \quad (4)$$

$$\sigma_\theta(r, \theta) = \frac{1}{2\sqrt{2\pi}r} \cos\frac{\theta}{2} [K_I(1 + \cos\theta) - 3K_H\sin\theta] \quad (5)$$

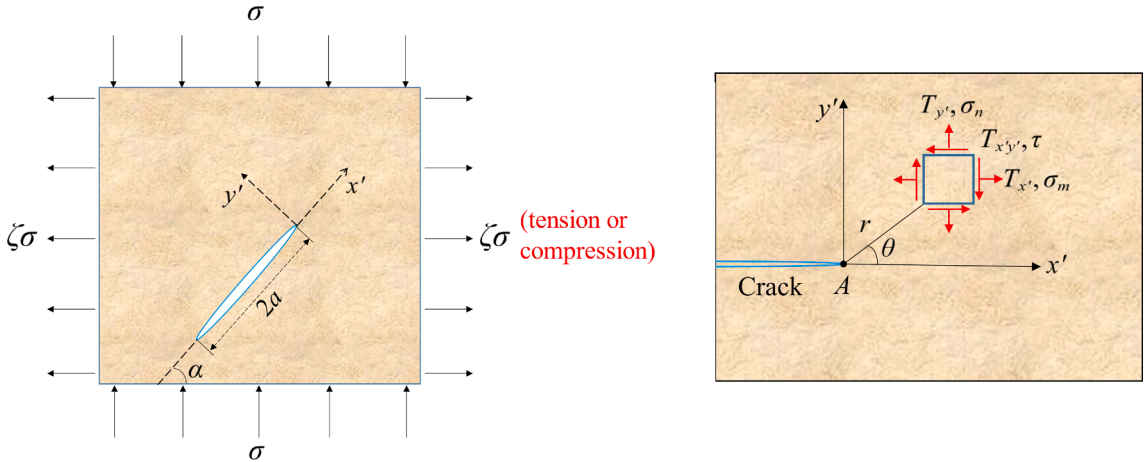


Fig. 6. (a) Stress status of an element with an inclined crack whose length is $2a$ and dip angle is α . $\sigma_v = \sigma_1 = \sigma$ is the vertical stress that contains the load from aquifer and upper strata, $\sigma_h = \sigma_3 = \zeta\sigma_v = \zeta\sigma_1 = \zeta\sigma$ is the horizontal stress where ζ is the lateral stress coefficient. (b) The local coordinate system $x'oy'$ and a sketch of the T-stress components.

$$\tau_{r\theta}(r, \theta) = \frac{1}{2\sqrt{2\pi}r} \cos \frac{\theta}{2} [K_I \sin \theta + K_{II} (3 \cos \theta - 1)] \quad (6)$$

where σ_r , σ_θ , and $\tau_{r\theta}$ are the radial stress, circumferential stress, and shear stress, respectively; K_I and K_{II} are mode I and mode II stress intensity factors that depend on the crack geometry and far-field stress components (σ_m , σ_n , and τ), which will be discussed in detail in the following paragraph.

We will distinguish the situation between $\sigma_n > 0$ (tension) and $\sigma_n \leq 0$ (compression) since when the crack is in compression, the crack surface will be closed, so it is not appropriate to use a negative K_I [21]. As a result, the formula for calculating K_I is given as

$$K_I = \max(\sigma'_n, 0) \sqrt{\pi a} \quad (7)$$

where $\sigma'_n = R_n \sigma_n$ is the reduced normal stress acting on crack and $R_n \in [0, 1]$ is the normal stress reduction factor. Similarly, we denote $R_s \in [0, 1]$ as the shear stress reduction factor and the shear stress acting on crack will be $\tau' = R_s \tau$. In Liu et al. [23], $1 - R_n$ is known as the normal transmitting factor and $1 - R_s$ is known as the shear transmitting factor. If $\sigma_n > 0$, the stress intensity factor of mode II is given as

$$K_{II} = \tau' \sqrt{\pi a} \quad (8)$$

While when $\sigma_n \leq 0$, we will consider the effective sliding stress τ_{eff} acting on the crack face, which is given by making an analogy with the frictional type of slip response

$$\tau_{eff} = \max(0, |\tau'| - f|\sigma'_n|) \operatorname{sgn}(\tau') \quad (9)$$

where f is the frictional coefficient on the crack surface and $\operatorname{sgn}(\cdot)$ is the sign function. By using τ_{eff} , K_{II} is simply calculated as

$$K_{II} = \tau_{eff} \sqrt{\pi a} \quad (10)$$

In fact, Eqs. (8), (10) could be combined into one equation, which is given as

$$K_{II} = \underbrace{\max\{0, |\tau'| - f|\min(\sigma'_n, 0)|\}}_{\tau_{eff}} \operatorname{sgn}(\tau') \sqrt{\pi a} \quad (11)$$

Now we can conclude that Eqs. (7), (11) are suitable for both compression and tension cases. In Liu et al. [23], they also considered the cohesion on the crack surface, while this can be easily incorporated into our framework by modifying the definition of τ_{eff} .

In classical fracture mechanics, only the singular stress term with $r^{-0.5}$ is considered, while the uniform non-singular stress term (known as the T-stress) and higher-order terms $O(r^{0.5})$ are always ignored [49]. However, many studies suggest that T-stress can affect the crack initiation and crack path stability [16, 29, 49]. In the early work, the conventional T-stress is widely regarded as the stress acting parallel to the crack tip in the x' -direction [9, 34], in other words, the classical T-stress only addresses the x' -component. In the more recent work [20, 29], both parallel and perpendicular (to the crack tip) non-singular stresses ($T_{x'}$ and $T_{y'}$) in the vicinity of crack tip are considered. In this study, we consider three components of the T-stress, namely $T_{x'}$, $T_{y'}$, and $T_{x'y'}$ [21, 47], as shown in Fig. 6, and the complete stress field near the crack tip is given as follows [20]

$$\tilde{\sigma}_r(r, \theta) = \sigma_r(r, \theta) + T_x' \cos^2 \theta + T_y' \sin^2 \theta + 2T_{x'y'} \sin \theta \cos \theta \quad (12)$$

$$\tilde{\sigma}_\theta(r, \theta) = \sigma_\theta(r, \theta) + T_x' \sin^2 \theta + T_y' \cos^2 \theta - 2T_{x'y'} \sin \theta \cos \theta \quad (13)$$

$$\tilde{\tau}_{r\theta}(r, \theta) = \tau_{r\theta}(r, \theta) + (T_y' - T_x') \sin \theta \cos \theta + T_{x'y'} \cos(2\theta) \quad (14)$$

According to Liu [21], Tang [29], and Zhao et al. [47], the T-stress takes the following value: $T_{x'} = \sigma_m$, $T_{y'} = \sigma_n$, and $T_{x'y'} = f\sigma_n$ where f is already used in Eq. (9).

To obtain the direction of crack initiation and the onset of crack growth, it is first necessary to define the fracture initiation criterion. The maximum tangential tensile stress (MTTS) is the most popular criterion [29], which states that the direction of crack initiation coincides with the direction of the maximum tangential stress $\tilde{\sigma}_\theta$ along a constant radius r_c around the crack tip. The constant radius r_c is known as the critical radius of the fracture zone [11], which is a material property and independent of specimen geometries [37]. For rock materials, r_c can be viewed as the size of the fracture process zone (FPZ) in front of the crack tip [37]. In general, the MTTS criterion provides good results for tensile fracture in most of brittle materials. It can be stated mathematically as

$$\tilde{\sigma}_\theta(r_c, \theta_i) \geq f_t; \quad \frac{d}{d\theta} \Big|_{\theta=\theta_i} \tilde{\sigma}_\theta(r_c, \theta) = 0; \quad \frac{d^2}{d\theta^2} \Big|_{\theta=\theta_i} \tilde{\sigma}_\theta(r_c, \theta) \leq 0 \quad (15)$$

where θ_i is the solved wing crack initiation angle and f_t is the tensile strength [4]. On the other hand, for the crack under combined shear and compression, the MTTS criterion should be replaced by the maximum shear stress magnitude (MSSM) criterion, especially under the condition of high confining pressure [11,29]. The MSSM criterion states that a shear crack will initiate at the location where the absolute value of the shear stress computed at a radial distance r_c attains its maximum, which can be stated mathematically as

$$\left| \tilde{\tau}_{r\theta}(r_c, \theta_i) \right| \geq \tau_t; \quad \frac{d}{d\theta} \Big|_{\theta=\theta_i} \left| \tilde{\tau}_{r\theta}(r_c, \theta) \right| = 0; \quad \frac{d^2}{d\theta^2} \Big|_{\theta=\theta_i} \left| \tilde{\tau}_{r\theta}(r_c, \theta) \right| \leq 0 \quad (16)$$

where τ_t is the shear strength. In general, the tensile strength of rock is generally smaller than its shear strength [29]. The last criterion is known as the minimum J_2 (second deviatoric stress invariant) criterion [48], in which J_2 of the stress field near the crack tip is given as

$$J_2 = \frac{1}{6} \left[\left(\tilde{\sigma}_r - \tilde{\sigma}_\theta \right)^2 + \left(\tilde{\sigma}_r - \tilde{\sigma}_z \right)^2 + \left(\tilde{\sigma}_\theta - \tilde{\sigma}_z \right)^2 \right] + \tilde{\tau}_{r\theta}^2 \quad (17)$$

where $\tilde{\sigma}_z$ is the stress component in the direction perpendicular to the $r\&\theta$ plane. For plane stress condition, we have $\tilde{\sigma}_z = 0$; while for plane strain condition, we have $\tilde{\sigma}_z = \nu (\tilde{\sigma}_r + \tilde{\sigma}_\theta)$ where ν is the Poisson's ratio. Since in our similar experiment, the physical model is a thin sheet, the plane stress condition is assumed [38]. Now the J_2 criterion can be described as: find a θ_i , such that it satisfies

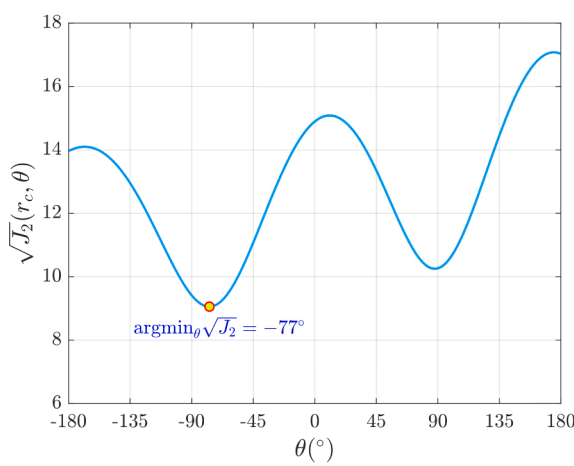


Table 3 Compressive shear stress and cracking angle of each loading condition during crack initiation

Condition	σ_x/MPa	σ_y/MPa	σ_x/σ_y	Cracking angle/(°)
1	2.71	6.13	0.44	-72
2	5.42	10.88	0.50	-76

From Wang et al. (2019) [30]



Fig. 7. Distribution of J_2 (MPa^2) around the crack tip under the loading condition #2 in [30]. Experimental results from [30] are attached on the right.

$$\frac{d}{d\theta} \Big|_{\theta=\theta_i} J_2(r_c, \theta) = 0; \quad \frac{d^2}{d\theta^2} \Big|_{\theta=\theta_i} J_2(r_c, \theta) \geq 0 \quad (18)$$

Finally, we give two benchmark examples to show the feasibility of our proposed analytical solution. The first example deals with the crack initiation and propagation under compression-shear load by using a single-edge symmetric double-crack specimen [30]. The specimen was loaded by a MTS biaxial material test system whose shaft displacements and forces can be adjusted freely during loading. Through the experiment, authors reported the crack initiation angles for six different loading conditions. The second example investigates crack propagation in flawed rock mass under uniaxial compression through DEM analyses [13]. In the first example, we assign σ_m , σ_n , and τ directly from the experimental data as $\sigma_m = 0$, $\sigma_n = -5.42$ MPa, and $\tau = -10.88$ MPa [30] (α is not needed). Other parameters are given as: $a = 0.005$ m, $f = 0.26$, $r_c = 1.296 \times 10^{-3}$ m, and $R_n = R_s = 1$. In the second example, we assume following parameters: $a = 8.915 \times 10^{-3}$ m, $\zeta = 0$, $f = 0.5$, $r_c = 1.296 \times 10^{-3}$ m, and $R_n = R_s = 1$. The verification results are shown in Fig. 7 and Fig. 8, which definitely confirm the rationality of the proposed theoretical model.

5. Results and discussions

5.1. Movement trend of the overlying strata and strata separation

During the process of model excavation, the collapse characteristics of the overlying strata are shown in Fig. 9. When the working face advanced to 40 cm, microcracks occurred in the middle of the direct roof (the 4th layer), and the lower part was slightly bent. When the working face advanced to 50 cm, the lower part of the direct roof collapsed, as shown in Fig. 9(a). When the working face advanced to 60 cm, the upper part of the direct roof was also broken. The caving height of the overlying strata reached 10.8 cm, the fracture angle of the strata on the cut side was 65°, and the fracture angle of the strata on the advancing side was 63°. The results are shown in Fig. 9(b).

When the working face advanced to 70 cm, a gap was formed between the 4th fine sandstone layer and the 5th coarse sandstone layer. This gap was relatively large, with a maximum development height of 2.1 cm and a strike length of 47.6 cm, as shown in Fig. 9(c). However, this gap was insufficient to store a certain amount of groundwater and could not lead to water inrush as it disappeared when the working face advanced to 80 cm.

When the working face advanced to 90 cm, a transverse crack was formed between the 8th siltstone layer and the 9th coarse sandstone layer. When the working face advanced to 110 cm, the transverse crack extended toward both sides and formed a bed separation space. This bed separation space was larger than the previous gap, with a maximum development height of 2.2 cm and a strike length of 61.2 cm, as shown in Fig. 9(d). At this moment, the fracture angle of the strata on the cut side was 68°, while it decreased from 63° to 57° on the advancing side. The 9th coarse sandstone layer retained a large amount of groundwater, which acts as the source of water for the bed separation space, and meanwhile, the hydraulic conductivity of the 8th siltstone layer was quite small. These conditions allowed the bed separation space to accumulate water, so the water injection test started at this stage. The detailed water accumulation process is given in the next subsection. Working face advancement was still executed as before. When the working face advanced to 120 cm, the bed separation space was further expanded, with a maximum development height of 3.3 cm and a strike length of 82.6 cm, as shown in Fig. 9(e). Subsequently, the water inrush accident occurred.

When the working face advanced to 140 cm, a transverse crack with a length of 33 cm was formed in the 9th coarse sandstone layer above the bed separation space. The height of the bed separation space decreased to 2.9 cm, while the strike length slightly increased. When the working face advanced to 150 cm, the coarse sandstone of the 9th layer suddenly broke within an hour, and the bed separation space almost disappeared, as shown in Fig. 9(f). Also from this figure, we find that more water-conducting fractures occurred on the advancing side than on the cut side underneath the bed separation space, which indicates that the water inflow is relatively high

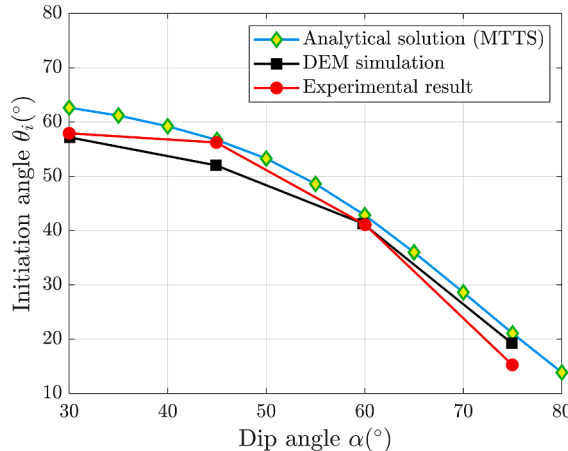


Fig. 8. Relationship between the pre-existing crack inclination and crack initiation angle obtained by different methods [13].



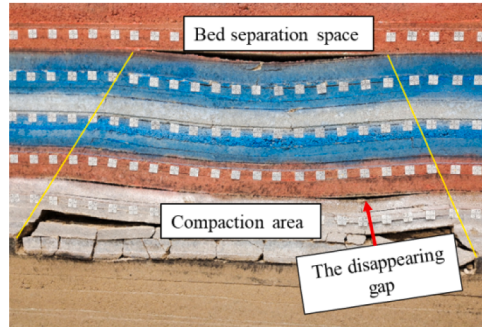
(a) Collapse of the lower part of the direct roof



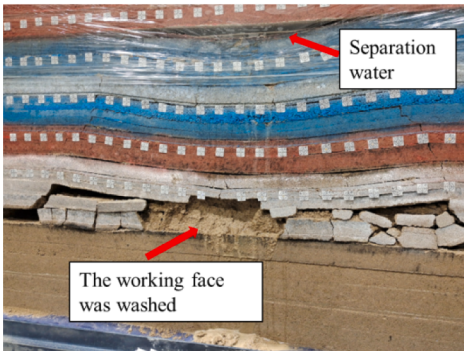
(b) Collapse of the upper part of the direct roof



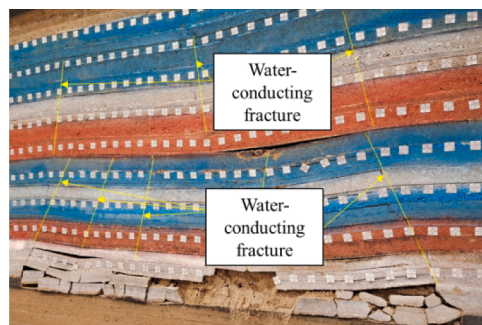
(c) Formation of a gap when the working face advanced to 70 cm



(d) Formation of a bed separation space that can accumulate water



(e) Water inrush accident and a relatively large bed separation space when the working face advanced to 120 cm



(f) Coarse sandstone was broken when the working face advanced to 150 cm and the bed separation space disappeared

Fig. 9. Failure characteristics of the overlying strata as the working face advanced. Some of these characteristics are qualitatively similar to those in Fig. 4 of [38], thus confirming the effectiveness of our experimental approach.

on the working face when separation water inrush occurs.

5.2. Analysis of water accumulation in the bed separation space and wing crack initiation

In this subsection, we would analyze the water accumulation process in detail. Firstly, we evaluate the possibility and potential direction of wing crack initiation. According to the experimental scheme, when the working face advanced to 110 cm, water was injected into the 9th coarse sandstone layer. The initial pump flow rate was set to be 300 mL/min, and when water appeared in the bed separation space, the pump flow rate was increased to 500 mL/min. In Fig. 10, we show the conditions of the 8th siltstone layer before and after the water injection, respectively. Some new cracks were generated due to the accumulated water in the bed separation space, and we want to analyze the initiation of these new cracks by using the theory in Section 4. To apply the analytical formulae, we would



Fig. 10. Conditions of the 8th siltstone layer. Left: before water injection. Right: after water injection.

simulate the water accumulation in the bed separation space as an increase in σ (see Fig. 6) for the element that contains an existing isolated crack [14]. The following material parameters have been adopted (calibrated) in the analytical calculations, as given in Table 2. In Fig. 11, we show the calculated wing crack initiation angle θ_i from the MSSM criterion and the corresponding $|\tau_{ir}(r_c, \theta_i)|$ when the dip angle α is in the range of 10° to 80° . We see that the maximum shear stress (in absolute value) is always proportional to σ . Therefore, when σ reaches a certain threshold, the wing crack will be initiated and propagate to the bed separation space under this stable σ . As for the direction, we see that the MSSM criterion always predicts a small $|\theta_i|$, which implies the wing cracks would propagate nearly align with the original direction. This is approximately consistent with our similar experiment result, i.e., a splitting failure (circled area in Fig. 10). These new cracks would act as main flowing channels during the subsequent water inrush process.

From the laboratory experiment, the complete process of water accumulation in the bed separation space can be divided into the following four stages, as shown in Fig. 12:

(a) Initial stage of the water accumulation process. During the water injection test, fluid flow mainly happened along two directions in coarse sandstone, namely horizontal and vertical directions. The horizontal fluid flow could increase the water content in the coarse sandstone layer, and the vertical flow driven by gravity would increase the amount of water accumulated in the bed separation space.

(b) Rapid growth stage of the water accumulation process. With an increase in the pump flow rate, the seepage velocity has been enhanced, which extended the range of regions with a high level of water abundance in the coarse sandstone layer and greatly promoted the water accumulation in the bed separation space.

(c) Maximum accumulated water stage. Under the combined action of mining stress and hydrostatic pressure, the fractures in siltstone were further developed, as described in the previous paragraph of this subsection. Even though the separation water could leave the bed separation space through these fractured channels, water in the coarse sandstone layer continued to flow into the bed separation space, resulting in the maximum amount of accumulated water in the bed separation space before the occurrence of the water inrush accident.

(d) Disaster-causing stage of the water accumulation process. In this stage, the damaged rock surrounding the fracture channel was gradually eroded by water, resulting in a high frequency of water and sand inrush into the lower working face. Although in our similar experiment, the water inrush was like a seepage process, when we take the similarity ratio into consideration, the actual process would be more severe. From Fig. 9(e)(f), we can see that the seepage velocity was quite large in our experiment, and its damage effect was pretty obvious. In addition, water was absorbed into the surrounding rocks, which eroded and disintegrated the material itself, and finally, the broken rock blocks were washed out and fell into the flume during the water inrush process.

5.3. Quantitative analysis of inrush water

At the end of the water inrush similar experiment, water was collected. A small peristaltic pump DIPump550-B253 was used in the

Table 2
Analytical parameters of model application to roof water inrush.

Name	Value	Note
Half crack length a before water accumulation (m)	0.4	The whole crack length $2a$ is about 1/10 of the thickness of the No. 8 stratum
Lateral stress coefficient ζ	0.4	Combined shear and compression, MSSM criterion should work
Frictional coefficient on the crack surface f	0.2 [21]	
Critical radius / Size of the FPZ r_c (m)	0.002 [4]	Also consistent with those in [29,37,47,49]
Dimensionless critical radius	$\sqrt{\frac{2r_c}{a}} = 0.1$	Good choice when considering T-stress according to [21,34]
Normal stress reduction factor R_n	0.7 [21]	
Shear stress reduction factor R_s	0.9 [21]	

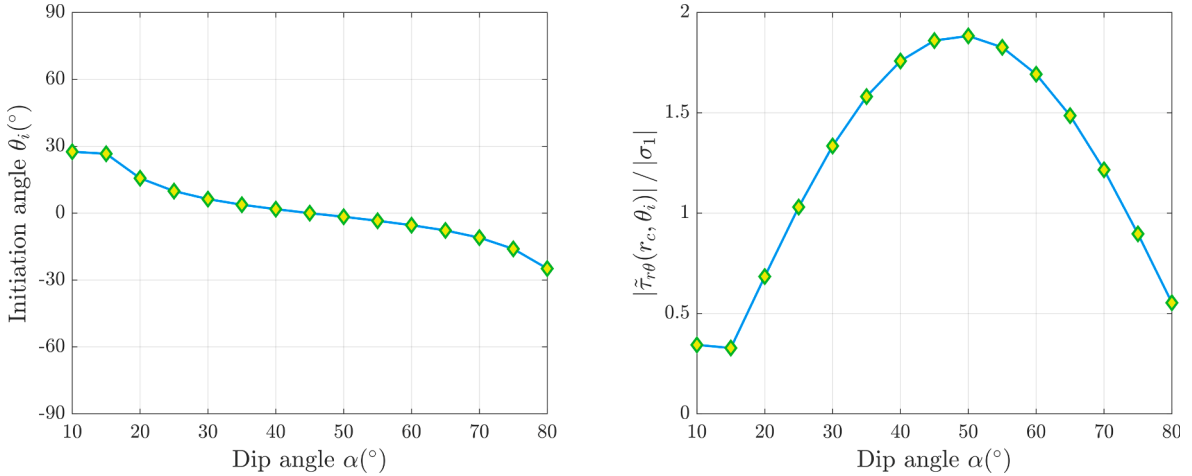


Fig. 11. Analytical results predicted by the MSSM criterion. Left: the relationship between θ_i and α . Right: the relationship between $|\tilde{\tau}_{r\theta}(r_c, \theta_i)|$ and α .

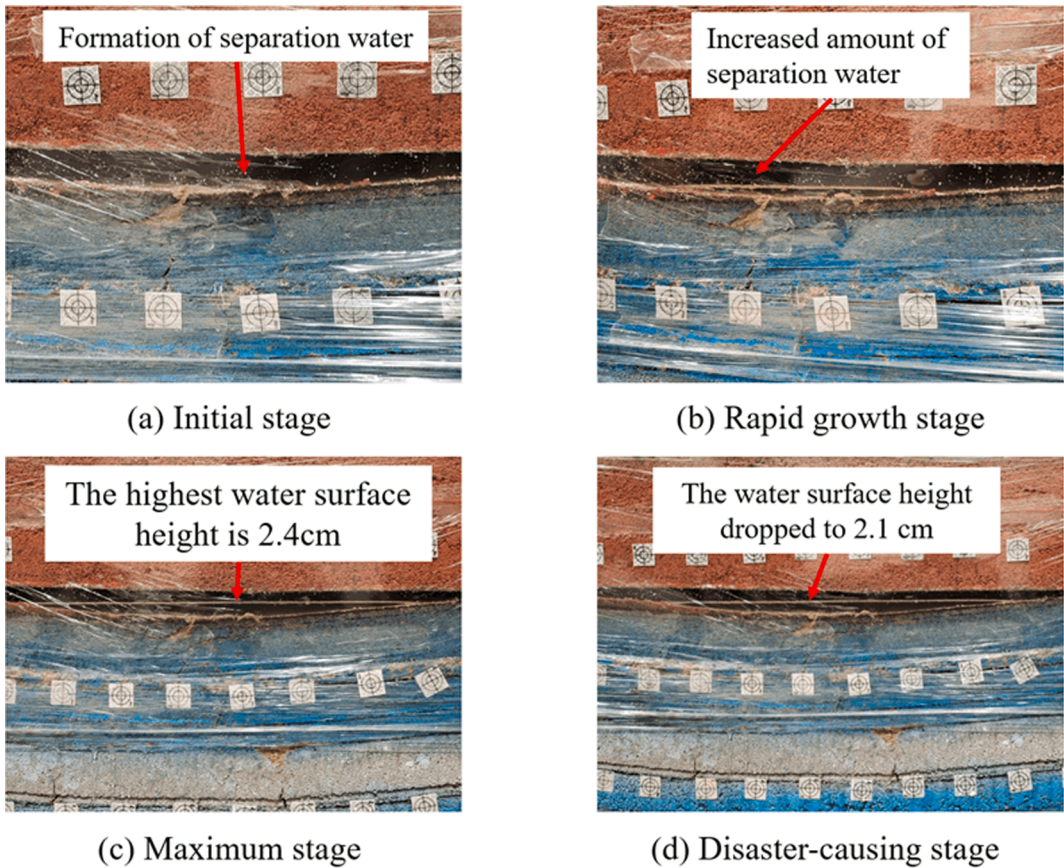


Fig. 12. Complete process of water accumulation in the bed separation space.

reverse operation mode to extract water from the collectors into the container. The collection process is shown in Fig. 13. The mass of water in the container was 8.3 kg, which was determined by an electronic scale. The mass of water injected through the pipeline was 20 kg. That is to say, the mass of water flowing toward the working face accounted for 41.5% of the total mass, which suggests that the injected water was partially retained in the rock strata, including the upper coarse sandstone (the 9th layer) and caving rock in the working face.



Fig. 13. Collection process of bed separation water from the collectors (left) into the container (right).

The rock strata containing water-conducting fractures between the working face and bed separation space were sampled to analyze water absorption in each rock stratum. The analysis is performed on the fine sandstone in layer 4, coarse sandstone in layer 5, and siltstone in layer 6, as shown in Fig. 14. We can see that in the 4th layer, namely, the direct roof, cemented rock was decomposed into fine particles with high water content and serious water erosion. For coarse sandstone existing in the water-bearing strata (the 5th layer), most of the particles were decomposed, and the water content was lower than that in the 4th layer. The 6th layer is a water-resisting rock stratum, and the particle surface was relatively dry with little erosion. Now we could conclude that the farther each rock stratum is away from the working face, the less erosion would occur in that stratum. The maximum water absorption and the most severe damage happened on the working face. All of these results are consistent with field observations, which confirm that similar materials with certain proportions could appropriately simulate water disasters.

6. Closure

The roof water inrush is always a big threat to the working face of a coal mine [25,39,44]. In this work, the process of water inrush due to roof bed separation was studied by similar simulation experiment and analytical wing crack initiation condition. After introducing the set-up of the experiment and the mathematical background of our analytical approach together with two verification examples, we apply the model to investigate the actual water inrush accident occurred in the 21805 working face of Yushujing coal mine. The results show that the evolution of bed separation space is a long-term process, and our analytical solution of wing crack initiation angle is approximately consistent with the experimental observation after water injection. By making use of the geometric similarity ratio, it is shown that when the advancing distance of the working face is 96 m, the separation water inrush occurred, which is supported by the field result (88.7 m). Besides, the location of the bed separation space (between the 8th and the 9th layers) and the role of the upper aquifer in our similar experiment also coincide with those in the field data from Zhiluo formation. The working face



(a) The 4th layer of fine sandstone (b) The 5th layer of coarse sandstone (c) The 6th layer of siltstone

Fig. 14. Water absorption analysis for three strata (from the 4th layer to the 6th layer) below the bed separation space and above the working face. The smaller the number, the lower the stratum.

was more prone to the damage caused by water inrush in our similar experiment, and this phenomenon also happened in the actual water inrush accident. To summarize, these results and approaches will help to provide scientific guidance for safe mining of working face with such risks.

Nevertheless, there are still some limitations in our approach. On the one hand, a 2D similar simulation experiment cannot fully reflect the actual 3D water inrush process due to the lack of a directional stress limit. As a result, the water pressure may not be measured accurately in our similar experiment. In addition, due to a small pore size, the laminar flow dominates the entire process, which is different from the actual water inrush (non-Darcy flow). On the other hand, the cracks in the field can be complicated with multiple initiation locations, which implies that Eqs. (4)–(6) are not fully accurate due to the crack interaction. In that situation, we could resort to the numerical methods such as the phase field method or the peridynamics approach.

Data availability statement

All data, models, or code generated or used during the study are available from the corresponding author upon reasonable request.

Declaration of Competing Interest

The authors declare that they have no known competing financial interests or personal relationships that could have appeared to influence the work reported in this paper.

Data availability

Data will be made available on request.

Acknowledgments

This work received support from the National Natural Science Foundation of China (51774199). The authors are grateful to 2 anonymous reviewers for their constructive comments. Their expert reviews have helped to improve the paper substantially.

References

- [1] L. Chen, Q. Ou, Z. Peng, Y. Wang, Y. Chen, Y. Tian, Numerical simulation of abnormal roof water-inrush mechanism in mining under unconsolidated aquifer based on overburden dynamic damage, *Eng. Fail. Anal.* 133 (2022), 106005.
- [2] W. Chen, W. Li, J. He, W. Qiao, Q. Wang, Y. Yang, Impact of mining-induced bed separation spaces on a cretaceous aquifer: a case study of the Yingpanhao coal mine, Ordos Basin, China, *Hydrogeol. J.* 30 (2) (2022) 691–706.
- [3] S. Dai, B. Han, S. Liu, N. Li, F. Geng, X. Hou, Neural network-based prediction methods for height of water-flowing fractured zone caused by underground coal mining, *Arabian J. Geosci.* 13 (12) (2020), 495.
- [4] H. Deng, M. Zhu, J. Li, Y. Wang, Q. Luo, X. Yuan, Study of mode-I fracture toughness and its correlation with strength parameters of sandstone, *Rock Soil Mech.* 33 (12) (2012) 3585–3591 (In Chinese).
- [5] K. Fan, W. Li, Q. Wang, S. Liu, S. Xue, C. Xie, Z. Wang, Formation mechanism and prediction method of water inrush from separated layers within coal seam mining: a case study in the Shilawusu mining area, China, *Eng. Fail. Anal.* 103 (2019) 158–172.
- [6] Y. Fei, S. Liu, Y. Xu, L. Zhao, Failure analysis of thin bedrock and clay roof in underground coal mining: case study in Longdong coal mine, *Int. J. Geomech.* 20 (10) (2020), 04020187.
- [7] H. Gui, M. Lin, X. Song, Identification and application of roof bed separation (water) in coal mines, *Mine Water Environ.* 37 (2) (2018) 376–384.
- [8] H. Gui, S. Tong, W. Qiu, M. Lin, Research on preventive technologies for bed-separation water hazard in China coal mines, *Appl. Water Sci.* 8 (1) (2018), 7.
- [9] M. Gupta, R.C. Alderliesten, R. Benedictus, A review of T-stress and its effects in fracture mechanics, *Eng. Fract. Mech.* 134 (2015) 218–241.
- [10] R. Hu, W. Shi, X. Zhai, K. Huang, Study on evolution characteristics of regenerated roof structure in downward mining of bifurcated coal seam, *Adv. Mater. Sci. Eng.* (2021), 8226616.
- [11] J. Huang, H. Tang, X. Pan, Z. Gan, W. Hua, S. Dong, Investigation of the compression-shear fracture propagation for rocks accounting for confining pressure and crack surface friction, *Theor. Appl. Fract. Mech.* 119 (2022), 103346.
- [12] Y. Ji, H. Cao, B. Zhao, Mechanism and control of water inrush from separated roof layers in the Jurassic coalfields, *Mine Water Environ.* 40 (2) (2021) 357–365.
- [13] M. Jiang, N. Zhang, Z. Shen, H. Chen, DEM analyses of crack propagation in flawed rock mass under uniaxial compression, *Rock and Soil Mechanics* 36 (11) (2015) 3293–3300 (In Chinese).
- [14] C. Li, J. Zuo, S. Xing, W. Du, X. Chuai, Failure behavior and dynamic monitoring of floor crack structures under high confined water pressure in deep coal mining: A case study of Hebei, China, *Eng. Fail. Anal.* 139 (2022), 106460.
- [15] H. Li, Q. Chen, Z. Shu, L. Li, Y. Zhang, On prevention and mechanism of bed separation water inrush for thick coal seams: a case study in China, *Environ. Earth Sci.* 77 (22) (2018), 759.
- [16] X.-F. Li, G.-L. Liu, K.Y. Lee, Effects of T-stresses on fracture initiation for a closed crack in compression with frictional crack faces, *Int. J. Fract.* 160 (1) (2009) 19–30.
- [17] Y.P. Li, C.H. Yang, Influence of geometric characteristics of pre-existing cracks on mixed mode fracture under compression-shear loading, *Chin. J. Rock Mech. Eng.* 25 (3) (2006) 462–466 (In Chinese).
- [18] W. Liang, Y. Zhao, J. Liu, D. Elsworth, Z. Feng, J. Cai, Advances in in-situ modified mining by fluidization and in unconventional geomechanics, *Adv. Geo-Energy Res.* 5 (1) (2021) 1–4.
- [19] Y. Liang, W. Sui, J. Qi, Experimental investigation on chemical grouting of inclined fracture to control sand and water flow, *Tunn. Undergr. Space Technol.* 83 (2019) 82–90.
- [20] H. Liu, Wing-crack initiation angle: A new maximum tangential stress criterion by considering T-stress, *Eng. Fract. Mech.* 199 (2018) 380–391.
- [21] H. Liu, Initiation mechanism of cracks of rock in compression and shear considering T-stress, *Chin. J. Geotech. Eng.* 41 (7) (2019) 1296–1302 (In Chinese).
- [22] S. Liu, S. Dai, W. Li, B. Han, B. He, J. Luo, A new monitoring method for overlying strata failure height in Neogene laterite caused by underground coal mining, *Eng. Fail. Anal.* 117 (2020), 104796.
- [23] T. Liu, P. Cao, H. Lin, Damage and fracture evolution of hydraulic fracturing in compression-shear rock cracks, *Theor. Appl. Fract. Mech.* 74 (2014) 55–63.

- [24] W. Qiao, W.P. Li, X.Q. Li, Mechanism of 'Hydrostatic water inrush' and countermeasures for water inrush in roof bed separation of a mining face, *J. Min. Safety Eng.* 28 (01) (2011) 96–104 (In Chinese).
- [25] W. Qiao, Z.W. Wang, W.P. Li, Y.G. Lyu, L.G. Li, Y. Huang, J.H. He, X.Q. Li, S.L. Zhao, M.N. Liu, Formation mechanism, disaster-causing mechanism and prevention technology of roof bed separation water disaster in coal mines, *J. China Coal Soc.* 46 (02) (2021) 507–522 (In Chinese).
- [26] W.Y. Shao, Critical rainfall intensity for safe evacuation from underground spaces with flood prevention measures, *J. Zhejiang University-Science A* 11 (9) (2010) 668–676.
- [27] Q. Sun, G. Meng, K. Sun, J. Zhang, Physical simulation experiment on prevention and control of water inrush disaster by backfilling mining under aquifer, *Environ. Earth Sci.* 79 (18) (2020), 429.
- [28] Y. Sun, P. Zhang, W. Yan, F. Yan, J. Wu, Compressive deformation characteristics of crushed sandstone based on multiple experimental factors, *Arch. Min. Sci.* 65 (1) (2020) 129–146.
- [29] S.B. Tang, The effect of T-stress on the fracture of brittle rock under compression, *Int. J. Rock Mech. Min. Sci.* 79 (2015) 86–98.
- [30] B. Wang, Y. Zhang, H. Zuo, H. Wang, Study on the influence of compressive stress on the compression shear crack propagation, *Chin. J. Theore. Appl. Mech.* 51 (3) (2019) 845–851 (In Chinese).
- [31] X. Wang, S. Zhu, H. Yu, Y. Liu, Comprehensive analysis control effect of faults on the height of fractured water-conducting zone in longwall mining, *Nat. Hazards* 108 (2) (2021) 2143–2165.
- [32] Y.Q. Wang, X. Wang, J.S. Zhang, B.S. Yang, W.J. Zhu, Z.P. Wang, Similar experimental study on retaining waterproof coal pillar in composite strata mining, *Sci. Rep.* 12 (1) (2022), 1366.
- [33] Z. Wang, Q. Zhang, J. Shao, W. Zhang, X. Wu, X. Zhu, New type of similar material for simulating the processes of water inrush from roof bed separation, *ACS Omega* 5 (47) (2020) 30405–30415.
- [34] J.G. Williams, P.D. Ewing, Fracture under complex stress - The angled crack problem, *Int. J. Fract.* 26 (4) (1984) 346–351.
- [35] L. Wu, H. Bai, D. Ma, Prediction and prevention of water inrush hazards from bed separation space, *Mine Water Environ.* 40 (3) (2021) 657–670.
- [36] M. Xing, W. Li, Q. Wang, D. Yang, Risk prediction of roof bed-separation water inrush in a coal mine, *China, Electronic J. Geotech. Eng.* 20 (1) (2015) 301–312.
- [37] J. Yang, H. Lian, W. Liang, V.P. Nguyen, Y. Chen, Experimental investigation of the effects of supercritical carbon dioxide on fracture toughness of bituminous coals, *Int. J. Rock Mech. Min. Sci.* 107 (2018) 233–242.
- [38] Q. Ye, G. Wang, Z. Jia, C. Zheng, W. Wang, Similarity simulation of mining-crack-evolution characteristics of overburden strata in deep coal mining with large dip, *J. Petrol. Sci. Eng.* 165 (2018) 477–487.
- [39] L. Yin, K. Ma, J. Chen, Y. Xue, Z. Wang, B. Cui, Mechanical model on water inrush assessment related to deep mining above multiple aquifers, *Mine Water Environ.* 38 (4) (2019) 827–836.
- [40] Q.G. Yu, H.X. Zhang, W.N. Deng, Y.P. Zou, Analysis of fault separation generation and its increasing effect on mining zone, *J. China Coal Soc.* 43 (12) (2018) 3286–3292 (In Chinese).
- [41] G. Zhang, H. Wang, S. Yan, C. Jia, X. Song, Simulated experiment of water-sand inrush across overlying strata fissures caused by mining, *Geofluids* (2020), 6614213.
- [42] Q. Zhang, Z. Wang, Spatial prediction of loose aquifer water abundance mapping based on a hybrid statistical learning approach, *Earth Sci. Inf.* 14 (3) (2021) 1349–1365.
- [43] S. Zhang, W. Guo, Y. Li, Experimental simulation of water-inrush disaster from the floor of mine and its mechanism investigation, *Arabian J. Geosci.* 10 (22) (2017), 503.
- [44] W.Q. Zhang, Z.Y. Wang, X.T. Wu, J.L. Shao, Y. Lei, X.N. Wu, Investigation and simulation on the model and prevention technology of water inrush from roof bed separation, *Coal Geol. Explorat.* 2021; 49(01):217-224+231 (In Chinese).
- [45] W. Zhang, Z. Wang, X. Zhu, W. Li, H. Yu, A risk assessment of a water-sand inrush during coal mining under a loose aquifer based on a factor analysis and the fisher model, *J. Hydrol. Eng.* 25 (8) (2020), 04020033.
- [46] J. Zhao, J. Chen, X. Zhang, J. Ning, Y. Zhang, Distribution characteristics of floor pore water pressure based on similarity simulation experiments, *Bull. Eng. Geol. Environ.* 79 (9) (2020) 4805–4816.
- [47] Y. Zhao, Y. Fan, Z. Zhu, C. Zhou, H. Qiu, Analytical and experimental study on the effect of T-stress on behavior of closed cracks, *Chin. J. Rock Mech. Eng.* 37 (6) (2018) 1340–1349 (In Chinese).
- [48] Y. Zhao, S. Xu, The minimum J2 criterion for I-II mixed mode brittle fracture, *Eng. Mech.* 19 (4) (2002) 94–98 (In Chinese).
- [49] D. Zhu, W. Du, A criterion for a hydraulic fracture crossing a frictional interface considering T-stress, *J. Petrol. Sci. Eng.* 209 (2022), 109824.
- [50] X. Zhu, Q. Zhang, W. Zhang, J. Shao, Z. Wang, X. Wu, Experimental study on the basic properties of a green new coal mine grouting reinforcement material, *ACS Omega* 5 (27) (2020) 16722–16732.